International Journal of Mechanical Sciences 272 (2024) 109295

Contents lists available at ScienceDirect

International Journal of Mechanical Sciences

journal homepage: www.elsevier.com/locate/ijmecsci

Localized plastic strain accumulation in shape memory ceramics under cyclic loading

Amirreza Lotfolahpour, Mohsen Asle Zaeem *

Department of Mechanical Engineering, Colorado School of Mines, 1500 Illinois street, Golden, CO 80401, USA

ARTICLE INFO

Keywords:
Phase-field modeling
Viscoplasticity
Data analysis
Cyclic loading
Shape memory ceramics
Polycrystals

ABSTRACT

The premature failure of shape memory ceramics (SMC)s under cyclic loading is a critical issue limiting their applications as actuators and thermal protection layers. Martensitic phase transformation (MPT), essential for superelasticity and shape memory functionalities in SMCs, induces localized plastic deformations due to phase expansion. In polycrystalline materials, the accumulation of localized plastic strain serves as the primary mechanism for fatigue crack initiation under cyclic loading. In this research, a phase-field (PF) phase transformation model coupled with a viscoplasticity model is presented to study the effects of microstructural features, engineered pores, and sample size on plastic strain accumulation (PSA) during cyclic loading of SMCs. Our findings highlight that the grain boundaries (GB)s are critical regions with high PSA, with noticeable reductions observed by decreasing the grain boundary density (GBD). Additionally, we found that engineered pores effectively reduced cyclic PSA, however, we identified a threshold on the volume fraction of pores. Also, textured microstructures with certain characteristics demonstrate significant influence on PSA. A cross-correlation data analysis approach is employed to study the relationship between the studied microstructural features and PSA to facilitate the identification of the most important factors controlling the irreversible PSA during compressive cyclic loading. By mitigating the rate of PSA, significant enhancements in cyclic life before fatigue crack initiation can be achieved, enabling superior performance in practical applications.

1. Introduction

Zirconia based SMCs are a class of smart materials that can be used as actuators, sensors, thermal protection layers, and energy dampers in a variety of industries such as aerospace and biomedical [1–4]. The underlying mechanism of superelasticity (SE) and shape memory effect (SME) behaviors in these materials is governed by MPT between two different crystallographic phases of tetragonal (*T*) and monoclinic (*M*). The shape change during MPT is associated with a large shearing and normal strains which cause large mismatch stresses mainly at phase interfaces and GBs [5]. The material must be able to accommodate these strains, otherwise after a few loading cycles, in the regions with large mismatch stresses, microscopic fatigue cracks initiate and propagate which then lead to a macroscopic failure.

In the macroscopic scale, these ceramics fracture at strains as low as 2 % which is lower than the full transformation strain about 7 % [5]. However, in microscopic samples, under certain microstructure configurations, multiple SE or SME cycles with full forward and reverse transformation can be observed [5,6]. For example, Lai et al. [5] made micropillars of ceria or yttria-stabilized zirconia ceramics with low number of grains and GBs through reducing the diameter of the micropillars, and in some of the samples they observed up to 53 complete SE cycles before fracture occurred. The underlying mechanism of crack initiation in these polycrystalline ceramics were reported to be the localized PSA mainly at GBs and phase interfaces [7–9]. SMCs are brittle and unable to fully accommodate the shape change due to MPT, and this can cause high mismatch stresses at GBs, phase interfaces, and around precipitates. The mismatch stresses cause local plastic strains originated from irreversible mechanisms such as GB sliding and dislocation activity [8]. In addition, both experimental [9] and numerical studies [10–12] well establish that the occurrence of MPT and plasticity is highly dependent on the crystallographic orientations of grains with respect to the loading direction [9–12]. Under cyclic loading, in the regions where plastic deformation originates, the PSA increases with each loading cycle and when it reaches a critical value, fatigue crack initiates [13–16]. Therefore, the PSA rate directly affects the fatigue life of materials and can be used as a fatigue indicator parameter to evaluate the number of loading cycles before fatigue crack initiation [16–18].

* Corresponding author.
E-mail address: zaeem@mines.edu (M. Asle Zaeem).

https://doi.org/10.1016/j.ijmecsci.2024.109295
Received 2 September 2023; Received in revised form 13 April 2024; Accepted 14 April 2024
Available online 16 April 2024
0020-7403/© 2024 The Author(s). Published by Elsevier Ltd. This is an open access article under the CC BY-NC-ND license (http://creativecommons.org/licenses/by-nc-nd/4.0/).

Computational studies can be used to further investigate the effects of the microstructural features such as grain orientation, GBD, and grain size (GS), as well as engineered pores on the plastic strain localization and accumulation in polycrystalline SE zirconia-based SMCs. Computational studies enable investigation of the effects of each microstructural feature separately and collectively which is difficult, if not impossible, by experimental studies. Among the previous models for studying microstructure evolution in materials, the PF approach has emerged as a powerful computational method that has been successfully applied to study MPT [12] and microstructure evolution in single crystal and polycrystalline shape memory alloys [19–22] and SMCs [23–27]. In this approach PF order parameters (OP)s represent the parent and product phases, and the shape change between parent and product phases is implemented through a stress-free strain tensor.

The PF approach or constitutive models coupled with plasticity models have been previously used to study the interaction between MPT and plastic deformations in shape memory materials, with a particular focus on NiTi alloys [28–37]. Among these studies, Yu et al. [30], proposed a crystal plasticity-based model to simulate MPT and plastic deformation in NiTi single crystals. Similar to experimental observations, their model predicted a high residual plastic strain during initial cycles and their model captured the effects of crystal orientation. Paranjape et al. [32] coupled a PF-MPT model with a crystal plasticity model to investigate the evolution of plastic deformation under cyclic thermal loadings. They studied the effects of plastic strain on MPT and transformation temperature. In a different study, Paranjape et al. [33] coupled PF-MPT with a rate-dependent crystal plasticity to simulate the interaction between slip plasticity and MPT in NiTi single crystal micropillars. They found a correlation between orientation of phase interface and dominating slip systems. Xie et al. [35], developed a crystal plasticity-based PF model and studied the cyclic behavior of a single crystal sample. They showed that plastic strain highly affects the stress-strain curve, and the accumulation occurs mainly along the phase interfaces. Xu et al. [36] coupled a PF-MPT model with a crystal plasticity model to study cyclic response of NiTi single crystals under thermal loads. They investigated the effects of plastic strain on forward and reverse MPT as well as martensite reorientation. Later on, Ju et al. [37] developed a comprehensive model that incorporates MPT and different types of plasticity, including slip. They predicted cyclic degradation in NiTi single crystal samples, and the obtained hysteresis loop and PSA was in good agreement with experiment.

The above studies on coupling MPT and plasticity in shape memory materials were focused on single crystal samples, limiting their ability to capture the effects of microstructural features such as GBs and grain size on the interaction between MPT and PSA. It is important to note that there have been some attempts to model the interaction between MPT and plasticity in polycrystalline samples [21,22,38–43]. For example, Xie et al. [21] utilized a crystal plasticity-based PF model and studied the cyclic behavior of polycrystalline NiTi samples under different loading rates. Additionally, Cisse and Asle Zaeem [22] studied the mechanical response and PSA in Cu-based SMAs under thermal loading. They predicted the stress-strain stabilization as well as cyclic plastic accumulation at GB triple junctions. In addition, they showed that plastic strain prevents complete shape recovery of the SMA in both SME and SE regimes. Xu et al. [41] proposed a crystal plasticity PF based model to study the cyclic degradation in polycrystalline NiTi samples. They observed an increasing irrecoverable cyclic plastic strain and examined the impact of plastic strain on the mechanical response of samples. Additionally, they studied the effects of strain rates and applied constant stress on the cyclic PSA. Chaugule and B.Le Graverend [42] developed a crystal plasticity-based model that incorporated mechanisms of MPT, transformation induced plasticity (TRIP), and viscoplasticity. They investigated the coupling between these mechanisms in single and polycrystal samples of a high temperature shape memory alloy (HTSMA). They successfully observed the progressive accumulation of viscoplastic strain versus number of thermal loading cycles similar to experimental observation. Kan et al. [43] developed a micromechanical model which included a viscoplasticity model to simulate cyclic response of HTSMAs. They applied cyclic thermal loadings and identified viscoplasticity as a primary irreversible mechanism in HTSMAs. Furthermore, their analysis revealed that viscoplasticity has a larger impact on the cyclic response under lower loading rates.

None of the studies investigating the interplay between MPT and plasticity in polycrystalline shape memory materials offer insights into the correlation between microstructural features, PSA, and fatigue crack initiation. Furthermore, these studies did not explore the influence of microstructural features on reducing PSA to enhance cyclic life prior to fatigue crack initiation. A recent study investigated the fatigue crack initiation and propagation in shape memory materials [16] by developing a TRIP-based fatigue model which incorporated TRIP accumulation as a fatigue indicator parameter for predicting low-cycle fatigue crack initiation in polycrystalline NiTi samples. They validated their model against experimental data. However, their study did not examine the effects of microstructural features on TRIP, and also it did not offer any strategies to reduce TRIP accumulation.

There have been studies on fatigue crack propagation modeling in macroscopic domains [44–49]. However, the majority of these studies lacked the inclusion of PSA which is a crucial phenomenon leading to fatigue crack initiation. Even when plasticity is considered, similar to microscale studies, none of previous studies provided insights into the fatigue crack initiation process or offered approaches to increase cyclic life before fatigue crack initiation by mitigating PSA.

In summary, previous works on coupling MPT with plasticity have not investigated the effects of microstructural features on the interaction between MPT and PSA in shape memory alloys and ceramics. Furthermore, none of these studies provided strategies to mitigate PSA to enhance cyclic life before fatigue crack initiation. In this research we aim to address these gaps by presenting a PF-based framework coupling PF-MPT with a viscoplasticity model to investigate the effects of the microstructural features on the plastic strain localization and accumulation in polycrystalline SMCs. To derive the viscoplasticity governing equations, we start from the total energy functional of the system and treat the plastic multiplier as an OP and minimize the total energy with respect to this OP. Then we demonstrate that with this approach we can recover the Bingham [50] viscoplasticity model. This approach yields a simple viscoplasticity model and we show that it predicts acceptable cyclic PSA that agrees with experimental results. The ideas and simulations presented in this work for reducing PSA have not been investigated in previous experimental or computational studies. The primary objective of this study is to provide guidance on mitigating PSA in order to enhance the cyclic life of SMCs before fatigue crack initiation.

The paper is structured as follows. In Section 2, the coupling between PF-MPT model and viscoplasticity model is presented in detail. Additionally, the PF approach to create polycrystals is elaborated at the end of this section. Section 3 provides details on the solution scheme, boundary conditions, materials properties, and model parameters. In Section 4, the simulation results, including stress-strain curves, MPT and equivalent plastic strain maps, and PSA plots are presented. In this section different potential ways to decrease the PSA during cyclic loading are studied. To provide additional clarity to the findings, a heatmap is generated to elucidate the correlation between microstructural features and PSA levels. Subsequently, conclusions are drawn in Section 5.

2. Phase-field model

This section first details the coupling between PF modeling of MPT and viscoplasticity. We start the formulation from the total energy functional of the system (F_{tot}) that includes all potential source and sink energies and proceed to elaborate on each energy term in detail. Subsequently, we express the governing equations and derive the OPs evolution equations using the Ginzburg-Landua relation and energy

minimization principles. In Section 2.2, we explain the PF approach to generate polycrystals and discuss the advantages of this approach compared to other approaches to create polycrystalline microstructures.

2.1. Coupling the PF of MPT and viscoplasticity

In PF-MPT, η_i are used as the OPs representing different phases in the system. $\eta_i = 0$ represents the T phase and $\eta_i = 1$ represents each of the two M variants in the c-a plane of zirconia. The F_{tot} can be written as:

$$F_{tot}(u_i,\ \eta_1, \eta_2,\ \ldots,\ \eta_m) = F_{el} + F_{ch} + F_{gd}\ + F_{pl}, \tag{1}$$

where F_{el} is the elastic strain energy, F_{ch} is the chemical free energy, F_{gd} is the gradient energy of the *T-M* or *M-M* interfaces, and F_{pl} is the energy dissipation due to plastic deformation. These energies are explained in detail in the following.

- Elastic strain energy (F_{el}):

F_{el} can be written as:

$$F_{el}(u_i) = \int_V \frac{1}{2} C_{ijkl}\varepsilon^{el}_{kl}\varepsilon^{el}_{ij} dV, \tag{2}$$

where u_i is the displacement, C_{ijkl} is the elastic tensor, and ε^{el}_{ij} is the elastic strain tensor which is defined as the difference between the total strain (ε^{tot}_{ij}), transformation strain (ε^{tr}_{ij}), and plastic strain (ε^{pl}_{ij}):

$$\varepsilon^{el}_{ij} = \varepsilon^{tot}_{ij} - \varepsilon^{tr}_{ij} - \varepsilon^{pl}_{ij}. \tag{3}$$

Considering a linear relation between the OPs and strains [23, 51–53], ε^{tr}_{ij} is defined as:

$$\varepsilon^{tr}_{ij} = \sum_{p=1}^{m} \varepsilon^{00}_{ij}(p)\eta_p, \tag{4}$$

where ε^{00}_{ij} is the stress-free strain tensor which represents the change in microstructure between parent and product phases [25]. The small strain assumption is considered and is defined as:

$$\varepsilon^{tot}_{ij} = \frac{1}{2}\left(u_{i,j} + u_{j,i}\right). \tag{5}$$

The difference between elastic constants in T and M phases is represented by the following linear relation [25]:

$$C_{ijkl}(\eta_1,\ \eta_2, \ldots,\ \eta_m) = \ C^T_{ijkl} + \sum_{p=1}^{m} \eta_p \left(C^M_{ijkl} - C^T_{ijkl}\right), \tag{6}$$

where C^T_{ijkl} and C^M_{ijkl} are elastic constants of the T and M phases, respectively. m is the number of product phases (monoclinic variants in this study). The elastic energy defined in Eq. (2) is based on the Hooke's law, therefore the stress tensor is related to elastic strain tensor through the following equation:

$$\sigma_{ij}\left(u_i, \eta_p\right) = C_{ijkl}(\eta_1,\ \eta_2, \ldots,\ \eta_m)\varepsilon^{el}_{kl}. \tag{7}$$

- Chemical free energy (F_{ch}):

F_{ch} determines the system's energy dissipation due to MPT. The 2–3-4 or 2–4-6 Landau polynomials defined in terms of OPs are the most common types of F_{ch} [12]. However, these chemical free energies underestimate the elastic response in the beginning of the stress-strain curve. Lotfolahpour et al. [23] proposed a modification to the 2–3-4 polynomial to address the elastic modulus underestimation, which is used in this paper:

$$F_{ch}(\eta_1, \eta_2, \cdots, \eta_m) = \int_V \Delta G\left(a\sum_{p=1}^{m}\eta_p^2 - b\sum_{p=1}^{m}\eta_p^3 + c\left(\sum_{p=1}^{m}\eta_p^2\right)^2 + d \times \sum_{p=1}^{m}|\eta_p|^n\right)dV; \quad 1 < n << 2 \tag{8}$$

where ΔG is the chemical driving force and is the difference in the specific F_{ch} between the parent and the product. The following equation can be used to calculate ΔG for 3Y-STZ at different temperatures [25, 54]:

$$\Delta G(T \rightarrow M) = -6159.18 + 6.98\mathrm{T}, \tag{9}$$

where the energy is in Jmol^{-1}(or Jm^{-3}) and the temperature (T) is in Kelvin (K). In addition, *a, b, c, d,* and *n* are coefficients that should be chosen in a way that maintains the value of the interfacial energy within the physical reasonable range [23] and at $\eta_p = 1$ result in $F_{ch} = \ \Delta G(T \rightarrow M)$.

- Gradient free energy (F_{gd}):

F_{gd} represents the interfacial energy between tetragonal-monoclinic or monoclinic-monoclinic phases and ensures a smooth transition of the OPs between different phases. It is expressed as:

$$F_{gd}(\eta_1, \eta_2,\ \ldots, \eta_m) = \ \int_V \frac{\mathrm{B}_{ij}}{2}\sum_{p=1}^{m}\nabla_i\eta_p\nabla_j\eta_p dV, \tag{10}$$

where ∇ is the gradient operator and B_{ij} is gradient energy tensor. We assume that the gradient energy coefficient is isotropic ($B_{ij} = B\delta_{ij}$) [25]. Therefore the Eq. (10) becomes:

$$F_{gd}(\eta_1, \eta_2,\ \ldots, \eta_m) = \ \int_V \frac{B}{2}\sum_{p=1}^{m}\left(\nabla\eta_p\right)^2 dV. \tag{11}$$

- Plastic energy (F_{pl}):

F_{pl} represents the system's energy dissipation due to plastic deformation, and it can be expressed as [55]:

$$F_{pl} = \int_V \int_0^{\varepsilon^{pl}_{eq}} \sigma_y\left(\varepsilon^{pl}_{eq}\right)d\varepsilon^{pl}_{eq}dV \tag{12}$$

where σ_y is the yield stress which is dependent on the equivalent plastic strain (ε^{pl}_{eq}) and is defined as:

$$\sigma_y = \sigma_{yo} + H\varepsilon^{pl}_{eq}. \tag{13}$$

σ_{yo} is the initial yield stress and H is the hardening coefficient.

- Governing equations

The evolution of the OPs representing the MPT can be obtained through Ginzburg-Landau relation [56,57]:

$$\frac{\partial\eta_p}{\partial t} = L\left(\frac{\delta F_{tot}}{\delta\eta_p}\right) = \ L\left(\frac{\delta F_{el}}{\delta\eta_p} + \frac{\delta F_{ch}}{\delta\eta_p} + \frac{\delta F_{gd}}{\delta\eta_p} + \frac{\delta F_{pl}}{\delta\eta_p}\right), \tag{14}$$

where L is the mobility parameter and controls the evolution rate of the OP η_p. The expansion of the above equation is:

$$\frac{\delta F_{\mathrm{el}}}{\delta \eta_p} = \frac{1}{2}\varepsilon_{ij}^{\mathrm{el}}\left(C_{ijkl}^{M} - C_{ijkl}^{T}\right)\varepsilon_{kl}^{\mathrm{el}} - \frac{1}{2}C_{ijkl}(\eta_1,\ \eta_2, \ldots,\ \eta_m)\varepsilon_{kl}^{00}(p)\varepsilon_{ij}^{\mathrm{el}} - \frac{1}{2}C_{ijkl}(\eta_1,\ \eta_2, \ldots,\ \eta_m)\varepsilon_{ij}^{00}(p)\varepsilon_{kl}^{\mathrm{el}}, \tag{15}$$

$$\frac{\delta F_{\mathrm{ch}}}{\delta \eta_p} = \vartriangle G\left(2a\eta_p - 3b\eta_p^2 + 4c\eta_p\sum_{p=1}^{m}\eta_p^2 + nd\left|\eta_p\right|^{n-1}\mathrm{sign}\left(\eta_p\right)\right) \tag{16}$$

$$\frac{\delta F_{\mathrm{gd}}}{\delta \eta_p} = -B\nabla^2\eta_p, \tag{17}$$

$$\frac{\delta F_{\mathrm{pl}}}{\delta \eta_p} = 0. \tag{18}$$

It is worth noted that in Eq. (15), the elastic strain ($\varepsilon_{ij}^{\mathrm{el}}$ and $\varepsilon_{kl}^{\mathrm{el}}$) is dependent on plastic strains (Eq. (3)). In other words, this equation shows how plasticity affects the evolution rate of η_p. In this paper to model plasticity, we consider an associative rate-dependent plasticity model. The plastic strain tensor is defined as:

$$\varepsilon_{ij}^{\mathrm{pl}} = \int_0^t \dot{\varepsilon_{ij}^{pl}}dt = \lambda N;\ N_{ij} = \frac{d\sigma_{mises}}{d\sigma_{ij}}, \tag{19}$$

where λ is the plastic multiplier and N_{ij} are the plastic flow directions [58]. The rate of the λ can be found through minimizing the F_{tot} with respect to λ. It should be noted that this approach is similar to deriving the evolution rate of OPs based on the Ginzburg-Landau relation in PF approach.

$$\frac{\partial \lambda}{\partial t} = \mu\left(\frac{\delta F_{\mathrm{tot}}}{\delta \lambda}\right) = \mu\left(\frac{\delta F_{\mathrm{el}}}{\delta \lambda} + \frac{\delta F_{\mathrm{ch}}}{\delta \lambda} + \frac{\delta F_{\mathrm{gd}}}{\delta \lambda} + \frac{\delta F_{\mathrm{pl}}}{\delta \lambda}\right), \tag{20}$$

where μ is the viscosity coefficient which controls the plastic strain evolution rate and plays the same role as L in Eq.(14), and the expansion of the above equation leads to:

$$\frac{\delta F_{\mathrm{el}}}{\delta \lambda} = -\frac{1}{2}C_{ijkl}(\eta_1,\ \eta_2, \ldots,\ \eta_m)N_{kl}\varepsilon_{ij}^{\mathrm{el}} - \frac{1}{2}C_{ijkl}(\eta_1,\ \eta_2, \ldots,\ \eta_m)N_{ij}\varepsilon_{kl}^{\mathrm{el}}, \tag{21}$$

$$\frac{\delta F_{\mathrm{ch}}}{\delta \lambda} = 0, \tag{22}$$

$$\frac{\delta F_{\mathrm{gd}}}{\delta \lambda} = 0, \tag{23}$$

$$\frac{\delta F_{\mathrm{pl}}}{\delta \lambda} = \sigma_{yo} + H\lambda|\boldsymbol{N}|. \tag{24}$$

The Eq. (21) presents the source terms for plastic strain evolution. In this equation the elastic constants are dependent on the tetragonal and monoclinic variants (η_p). In addition, the elastic strain ($\varepsilon_{ij}^{\mathrm{el}}$ and $\varepsilon_{kl}^{\mathrm{el}}$) is dependent on the transformation strain ($\varepsilon_{ij}^{\mathrm{tr}}$) and consequently on η_p. These dependencies reveal the coupled relationship between plasticity and MPT and shows that the evolution of the η_p affects the elastic constants and elastic strain and consequently the evolution of plastic strain. In addition, in Eq. (24), λ is ε_{eq}^{pl}. In order to make the plastic strain evolve only when stresses exceed the yield stress, we impose the Kuhn-Tucker conditions [59]:

$$\frac{\delta F_{\mathrm{tot}}}{\delta \lambda} \leq 0,\ \frac{\partial \lambda}{\partial t} \geq 0,\ \left(\frac{\delta F_{\mathrm{tot}}}{\delta \lambda}\right)\left(\frac{\partial \lambda}{\partial t}\right) = 0. \tag{25}$$

The plastic strain rate can be expressed as:

$$\dot{\varepsilon_{ij}^{\mathrm{pl}}} = \frac{\partial \lambda}{\partial t}\boldsymbol{N}\ . \tag{26}$$

This expression can be inserted in Eq. (19) to calculate the $\varepsilon_{ij}^{\mathrm{pl}}$. It is worth mentioning, this associative rate-dependent plasticity model resembles Bingham viscoplasticity model [50,58]. Furthermore, the average plastic strain is calculated through:

$$\left|\overline{\varepsilon^{\mathrm{pl}}}\right| = \frac{1}{A_{total}}\int_A \varepsilon_{eq}^{pl}dA \tag{27}$$

where A_{total} is the total domain area and A is the doamin of study in a 2D model. It is worth noting that in 3D doamins domain volume V must be used instead of A. In addition, by neglecting the body forces, the mechanical equilibrium equations lead to:

$$\mathrm{div}\,\sigma(u_i,\ \eta_i) = 0 \tag{28}$$

2.2. Generating polycrystals

This subsection explains our approach for creating polycrystals with different grain sizes. In addition, we explain the advantages of this approach in terms of discretization compared to other methods for creating polycrystals. To generate polycrystals, we use the PF grain growth model [60]. In this approach, a polycrystalline microstructure can be described by many field variables which each variable represents a grain and its orientation, and these variables are continuous in space. The temporal evolution of these field variables is described by the Ginzburg-Landau relation. This approach can create realistic polycrystals and overcomes the difficulties of generating high quality mesh due to the presence of lines (GBs) and GBs junctions when the grains and GBs are drawn manually or when the topology of the microstructure is directly imported to the numerical model.

We first create polycrystals without considering MPT, plasticity or any other physics. In this approach an OP ξ_i represents the ith grain in the domain. The total energy of the system can be expressed as following [60]:

$$F(\xi_i) = G\int_V\left(f + \sum_{i=1}^{s}\frac{k_i}{2}(\nabla\xi_i)^2\right)dV, \tag{29}$$

$$f = \sum_{i=1}^{s}\left(-\frac{\alpha}{2}(\xi_i)^2 + \frac{\beta}{4}(\xi_i)^4\right) + \gamma\sum_{i=1}^{s}\sum_{j\neq i}^{s}\xi_i^2\xi_j^2, \tag{30}$$

where V is the domain volume, α, β and γ are the model constants, G is the energy barrier, k_i are the gradient energy coefficients which directly determine the width of smeared interface between grains, and s is the total number of the grain orientations. It worth mentioning that the number of grains in the domain could be different than s depending on the initial conditions and the model parameters. The evolution equations of the OPs are obtained based on the Ginzburg-Landau relation [56,57] and are provided below:

$$\frac{d\xi_i}{dt} = \vartheta G\left(-\alpha\xi_i + \beta\xi_i^3 + 2\gamma\sum_{i=1}^{s}\sum_{j\neq i}^{s}\xi_i\xi_j^2 + k_i\nabla^2\zeta_i\right); i\ \&\ j = 1, 2, \cdots, s;\ i \neq j, \tag{31}$$

where ϑ is the mobility parameter and controls the evolution rate of the OPs.

3. Solution scheme and model parameters

In this section, first the details of the solution scheme are presented. Then, we describe the boundary conditions, the second and forth order tensors rotation, and the model parameters.

3.1. Solution scheme and boundary conditions

The governing equations presented in the previous section are solved in a finite element framework using the solid mechanics and mathematics modulus of COMSOL Multiphysics. First, we only solve the PF

polycrystal equations to produce the polycrystalline models (grain geometries). In this step, mechanical loads are not applied. We consider the number of OPs s (*s* in Eq. (29)-(31)) to be 30. In addition, to have a non-zero solution, we apply an initial randomly distributed value between 0 and 0.1 for each OP. After obtaining the polycrystalline structure, we assign an orientation to each grain and use the model for studying MPT under cyclic loading.

The governing equations of MPT, plasticity model, and mechanical equilibrium are solved by applying a cyclic displacement-controlled loading. Furthermore, the plane stress condition is considered in all these 2D simulations. The dimensions of the models and their boundary conditions are shown in Fig. 1. Based on this figure, rollers are applied on the bottom and left edges to avoid PSA at the sample boundaries.

For all models, quadrilateral elements are generated by the mapped mesh algorithm feature in COMSOL. A mesh study is conducted, a mesh size of 0.04 mm (or 10,000 quadrilateral elements in the domain) is found to be sufficient to resolve the interface of different OPs. Discretizing the samples with more elements did not noticeably change the microstructure, PT, PSA rate, and mechanical response, therefore we used 10,000 quadrilateral elements. The polycrystalline PF equations and the martensite PF and plasticity equations are solved using the "General Form PDE" module of COMSOL with linear shape functions. The displacements are solved using the Solid Mechanics module with quadratic shape functions. The staggered scheme [61] is used to solve the governing equations where nonlinear sub-problems are solved with Newton's method. A time step of 0.1 s is used for all simulations.

It should be noted that in Fig. 1(a) θ defines the grain orientation with respect to the global coordinates and measures positive counterclockwise. When $\theta = 0^\circ$, the a_t axis and c_t axis of the tetragonal phase are aligned with *x* axis and *y* axis respectively. In addition, in this paper, $\theta = 0^\circ$ corresponds to [010] oriented crystal. The following equations will be used to transfer the local stress-free strain tensor ($\varepsilon_{ij}^{00}(p)$) and local elastic stiffness tensor ($C_{mnop}(\eta_1, \eta_2, \ldots, \eta_m)$) to the global coordinate system:

$$\varepsilon_{ij}^{G00}(p) = R_{ik}R_{jl}\varepsilon_{ij}^{00}(p), \tag{32}$$

$$C_{ijkl}^{G} = R_{im}R_{jn}R_{ko}R_{lp}C_{mnop}, \tag{33}$$

R_{ij} is the rotation matrix for a grain with an orientation angle of θ, which in 2D is defined as:

$$R_{ij} = \begin{bmatrix} \cos(\theta) & \sin(\theta) \\ -\sin(\theta) & \cos(\theta) \end{bmatrix}. \tag{34}$$

3.2. Material properties and model parameters

This subsection details the mechanical properties of the material under investigation, model parameters, and the methodology for calculating the energy difference between the *T* and *M* phases. It is worth mentioning that the rationale behind selecting the value of μ in the viscoplasticity model is discussed in Section 4. 3Y-STZ, which is a SMC [7,62], is the material of study in this work. The equilibrium temperature of 3Y-STZ is reported to be ~883 K [25]. We consider the temperature of the system is constant and equal to 905 K and we use this temperature to calculate ΔG in Eq. (9) which yields $\Delta G = 156 \quad \mathrm{Jmol}^{-1}$ ($7.2 \times 10^6 \quad \mathrm{Jm}^{-3}$). It is worth noting that the considered temperature is higher than the equilibrium temperature, therefore, the system is in SE regime (strain recovery occurs after unloading without a need for temperature change). Eq. (35) and Eq. (36) show the stiffness tensor of tetragonal and monoclinic phases, respectively [63,64]. In addition, the stress-free strain tensors of two monoclinic variants in $a - c$ plane are given in Eqs. (37) and (38) [11,65]:

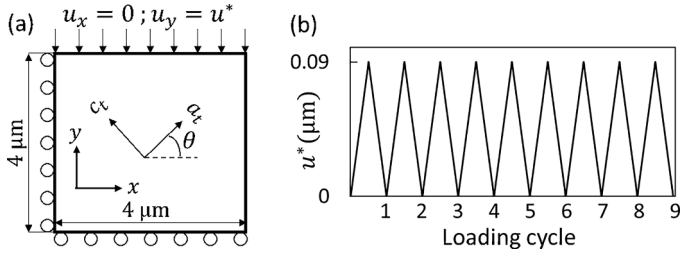

Fig. 1. (a) Domain dimensions and boundary conditions, and (b) applied displacement versus loading cycle.

$$C_{ijkl}^{T} = \begin{bmatrix} 361 & 100 & 62 & 0 & 0 & 0 \\ 100 & 361 & 62 & 0 & 0 & 0 \\ 62 & 62 & 264 & 0 & 0 & 0 \\ 0 & 0 & 0 & 59 & 0 & 0 \\ 0 & 0 & 0 & 0 & 59 & 0 \\ 0 & 0 & 0 & 0 & 0 & 64 \end{bmatrix} \mathrm{GPa}, \tag{35}$$

$$C_{ijkl}^{M} = \begin{bmatrix} 327 & 142 & 55 & 0 & 0 & -21 \\ 142 & 408 & 196 & 0 & 0 & 31 \\ 55 & 196 & 258 & 0 & 0 & -18 \\ 0 & 0 & 0 & 100 & -23 & 0 \\ 0 & 0 & 0 & -23 & 81 & 0 \\ -21 & 31 & -18 & 0 & 0 & 126 \end{bmatrix} \mathrm{GPa}, \tag{36}$$

$$\varepsilon_{ij}^{00}(1) = \begin{bmatrix} 0.0419 & -0.0761 \\ -0.0761 & -0.0181 \end{bmatrix}, \tag{37}$$

$$\varepsilon_{ij}^{00}(2) = \begin{bmatrix} 0.0419 & 0.0761 \\ 0.0761 & -0.0181 \end{bmatrix}. \tag{38}$$

Table 1 shows the other model parameters used in the simulations.

It should be noted that we select α, β, γ in the PF polycrystal model in a way that the shape of the source energy, *f* in Eq. (29), is a double well, and the value of *f* at $\zeta = 1$ is negative and lower than *f* at $\zeta = 0$. This makes $\zeta = 1$ the most stable phase in the system and ζs start to evolve upon starting the simulation if the initial value is slightly larger than zero. In addition, the k_i determine the interface thickness and must be selected small enough to guarantee a reasonable and physical thickness for the interfaces (the transition thickness from one OP to another OP). In appendix A, the interface thickness calculation for a 1D steady state case is explained in detail.

4. Results and discussion

First, the cyclic stress-strain curves and the PSA for a polycrystalline model with random grain orientations are presented. The findings from this initial model serve as the primary reference for evaluating the results of other models with different microstructural features. In the subsequent subsections, different strategies to mitigate PSA are investigated. At the end of this section and to further elucidate the findings of

Table 1
Model parameters.

Parameters	Values
a, *b*, *c*, *d*, and *n* in Eq. (8)	2.64, 10.04, 5.37, 3.05, and 1.1 [23]
σ_{y0} and *H* in Eq. (13)	3000MPa and 10GPa [25]
B in Eq. (11)	$1 \times 10^{-9} \quad \mathrm{Jm}^{-1}$ [25]
L in Eq. (14) and μ in Eq. (20)	$5 \times 10^{-9} \quad \mathrm{Pa}^{-1}\mathrm{s}^{-1}$ [23] and $3.3 \times 10^{-13} \quad \mathrm{Pa}^{-1}\mathrm{s}^{-1}$
α, β, γ, k_i, and G in Eqs. (29) and (30)	1, 1, 1, $1.875 \times 10^{-16} \quad \mathrm{m}^2$, and 1Pa
ϑ in Eq. (31)	$2 \quad \mathrm{Pa}^{-1}\mathrm{s}^{-1}$

this research, we conduct a cross-correlation data analysis to demonstrate the correlation between microstructural features, PSA, and MPT fraction.

To create the polycrystalline models, we only solve the polycrystal PF equation (Eq. (29) - Eq. (31)), and Fig. 2(a) depicts the obtained microstructure. To make the OPs (ζ_i) evolve, we consider a random distribution of initial values larger than zero and smaller than 0.1 for each OP. The average GS is 0.35μm. A range of 0.2μm to 2μm has been reported for 3Y-STZ GS experimentally [66]. After obtaining the microstructure, a random orientation (RO) between 0 ° and 90° is assigned to each OP ζ_i. The total length of GBs in this microstructure is about 84μm, and we calculate the GBD by dividing the total length of GBs by the total area of 16 μm^2, which yields 5.3 μm^{-1}. For more details on the GB length and GBD calculation see Appendix A. It is worth mentioning that by changing ϑ in Eq. (31), the number of grains and the average GS can be controlled. The microstructure obtained from this step is used in the simulations where the effects of microstructural features on the MPT, mechanical response, and PSA are studied. To study the texture effects, models with different grain orientations are built, which are described later in this section.

We start with the initial model shown in Fig. 2(a) to study the effects of grain orientation, GBD and pores on the PT and PSA under cyclic compressive loading. The mechanical response for cycle 1 (C1), 3 (C3), 7 (C7), and 9 (C9) is presented in Fig. 3. In the stress-strain plot, the stress refers to the absolute value of average stress in the loading direction (σ_y) and the strain refers to absolute value of engineering strain in the loading direction (ε_y). From C1 to C7, after each cycle the forward transformation starting stress decreases and the hysteresis loop becomes narrower. However, there is not a notable difference between hysteresis loops of C7, C8 (not plotted) and C9. In other words, the system stabilizes (known as training effect [6,67]) after 7 cycles. This behavior was experimentally observed in other shape memory materials [67]. Depending on the material properties and boundary conditions, the number of cycles after which stabilization happens can widely change. Lai et al. [5], reported 10 cycles for a coarse-grained zirconia-based SE SMC micropillar under compressive loading. Du et al. [6], reported 81 cycles before the stabilized hysteresis loop was observed in a single crystal zirconia-based spherical sample under compression loading.

Fig. 3 also displays the MPT at the beginning of loading (I), end of loading (II), and the end of unloading (III) of C9. Both monoclinic variants are present at the end of loading (II), and since the system is in the SE regime, after unloading most of the transformed regions transform back to the tetragonal phase. However, there are some regions that do not transform back. This occurs due to PSA near or at GBs. The plastic strain causes the accumulation of residual stress upon unloading and consequently, pockets of martensite are left behind. This process occurs in each cycle. In addition, at the end of loading, the grains with an angle between 10° and 60° show MPT and grains with an angle outside this range do not show noticeable MPT.

Fig. 4 presents the plot of average PSA ($\left|\overline{\varepsilon^{pl}}\right|$ Eq. (27)) in percent over the entire domain. There is a PSA of 0.047 % after C1, and the accumulation rate decreases in each additional cycle. This observation is consistent with experimental results of PSA in polycrystalline materials under cyclic loadings [38,68]. $\left|\overline{\varepsilon^{pl}}\right|$ keeps on accumulating in each cycle even after C7 ($\left|\overline{\varepsilon^{pl}}\right|$ = 0.074 %) after which the mechanical response stabilizes. This explains the fatigue failure in these materials. In other words, when polycrystalline materials including ceramics are under cyclic loading, with each additional cyclic loading not only new plastic sites emerge, but also in the regions that already experienced plastic deformation, the plastic strain keeps on increasing until it locally reaches a critical value after which microscopic fatigue cracks can initiate. Then the microscopic fatigue cracks start to grow until total failure happens. In addition, the cyclic plastic strain in these ceramics is a result of the accumulation of irreversible mechanisms such as slip [9] and GB sliding [26] which we model these mechanisms by a general von mises based viscoplasticity model. Since SMCs are brittle, the number of cycles from fatigue crack initiation to total failure is very limited [6], and if the fatigue crack initiation is delayed by reducing the PSA, their lifetime can increase significantly. It is worth mentioning that the PSA starts from 0.047 % after C1 and reaches 0.094 % at the end of C9. These values are in good agreement with the residual strain shown in experimental cyclic stress-strain curves [5]. This also confirms that the value of μ in the viscoplasticity model is reasonable. It is worth mentioning, to find a proper value for μ, we used stress-strain curves reported by deformation experiments of few grains micropillars [5]. We ran few grains simulations and tried different μ to produce reasonable stress-strain curves with a focus on values of cyclic PSA.

Fig. 4 also shows the equivalent plastic strain distribution (ε_{eq}^{pl}) in the domain at the end of C1, C3, and C9. The PSA is highest in triple junctions of GBs and keeps on increasing in each cycle. It is worth noting that plastic strain occurs at phase interfaces as well, however, its magnitude is considerably smaller compared to plastic strain at GBs. This observation holds true for all subsequent simulations. This cyclic increase of plastic strain is consistent with experimental materials [38] and numerical [31] studies on cyclic response of polycrystalline shape memory materials. This means triple junctions are critical sites that fatigue cracks possibly initiate from and lead to intergranular cracks. These results are consistent with experimental observation of fracture in SMCs [6,69]. The PSA can be used as a parameter to compare the cyclic life before fatigue crack initiation in different cases [17,18]. In the following, we aim to study different microstructural features such as grain orientation, GBD, and pores in order to reduce the overall PSA in the polycrystalline samples.

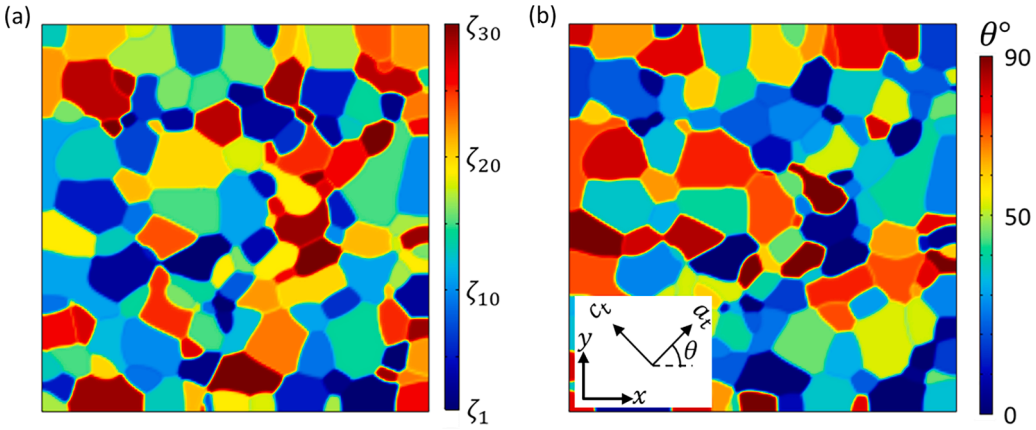

Fig. 2. (a) The obtained microstructure using 30 OPs in Eq. (29), and (b) Random orientations are assigned to grains.

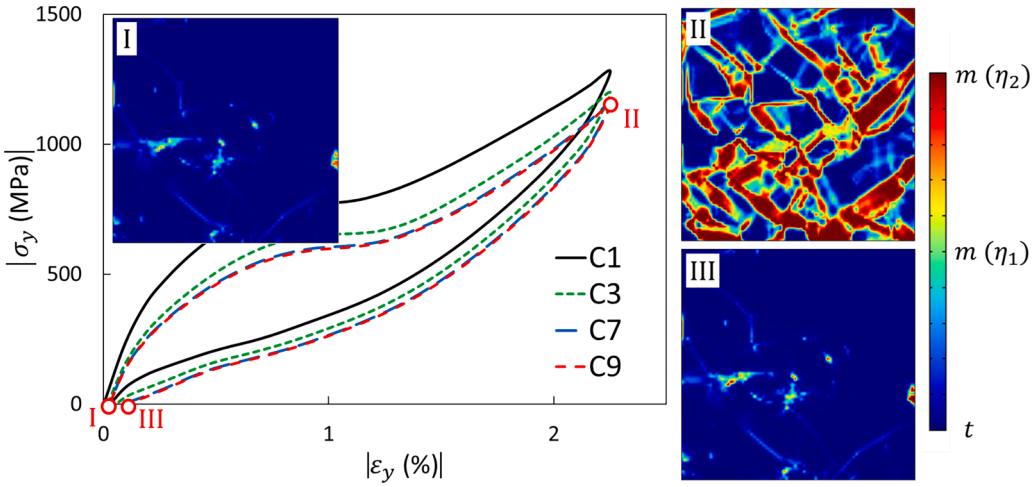

Fig. 3. Mechanical response ($|\boldsymbol{\sigma_y}|$ vs. $|\boldsymbol{\varepsilon_y}|$) of C1, C3, C7, and C9; MPT map at the beginning (I), end of loading (II), and end of unloading (III) of C9.

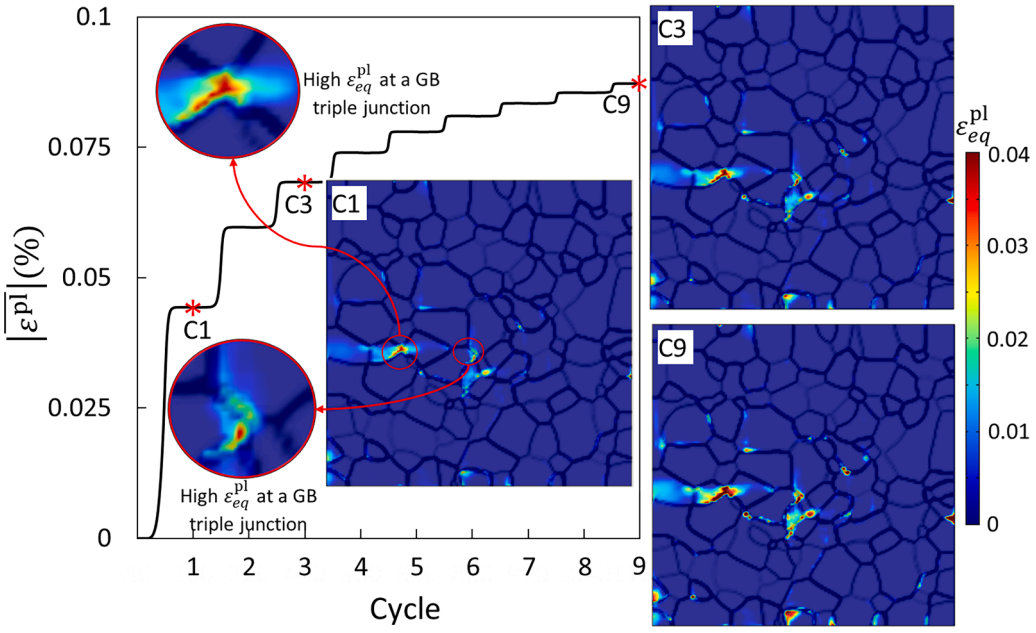

Fig. 4. PSA plot; Equivalent plastic strain maps are shown at the end of unloading of C1, C3 and C9.

4.1. *Effects of grain boundary density*

Based on the results presented in Fig. 4, GBs are critical sites at which plastic strain is highest. Therefore, through reducing the GBD, the PSA can be mitigated. In this subsection, we explore the effects of GBD through two different approaches. In the first approach, we reduce the GBD by cutting two small sub domains (S1 and S2) of 1μm × 2μm from the initial model. These sub domains are shown in Fig. 5. In these sub domains the average GS remains the same as the initial model, which is 0.35μm. In addition, the grain orientations remain random in both S1 and S2. The calculation of the GBD leads to 3.8 μm^{-1} and 3 μm^{-1} for S1 and S2, respectively. Fig. 5 shows the comparison of the $|\overline{\varepsilon^{pl}}|$ in these sub domains with the initial model. The inset figures in the bottom of Fig. 5(a) show the MPT in both sub domains at the end of loading of C9. In both S1 and S2, the $|\overline{\varepsilon^{pl}}|$ is predicted to be lower than the initial model (4μm × 4μm). This result suggests that by reducing the GBD through making the sample size smaller, $|\overline{\varepsilon^{pl}}|$ can be mitigated noticeably. One can also expect that for larger samples, a lower GBD will result in lower $|\overline{\varepsilon^{pl}}|$.

Few experimental studies also investigated the effects of GBD on the fatigue life of zirconia-based SMCs. Lai et al. [5] produced ceria and yttria stabilized zirconia micropillars with fewer grains and GBs by reducing the diameter of micropillars, and they applied cyclic compressive and bending loadings to the samples. They observed large strains up to 7 % and the ability to cycle reversibly through the MPT up to 50 cycles before failure occurs. Furthermore, Du et al. [6] produced oligocrystalline and single crystal spherical samples to mitigate the cracking problems in cyclic loading of polycrystalline zirconia-based SMCs. The reduced number of grains and GBs as well as lowering the diameter of the spherical samples resulted in lowering the GBD. They were able to observe up to 110 SE cycles in some samples with a diameter less than 4μm under cyclic compressive loading. We can conclude that model prediction is consistent with experimental observations and the PSA is an effective indicator of cyclic life in polycrystalline materials.

In the second approach for studying the effect of GBD, we produced coarse-grained microstructure by increasing the GS to reduce GBD. To

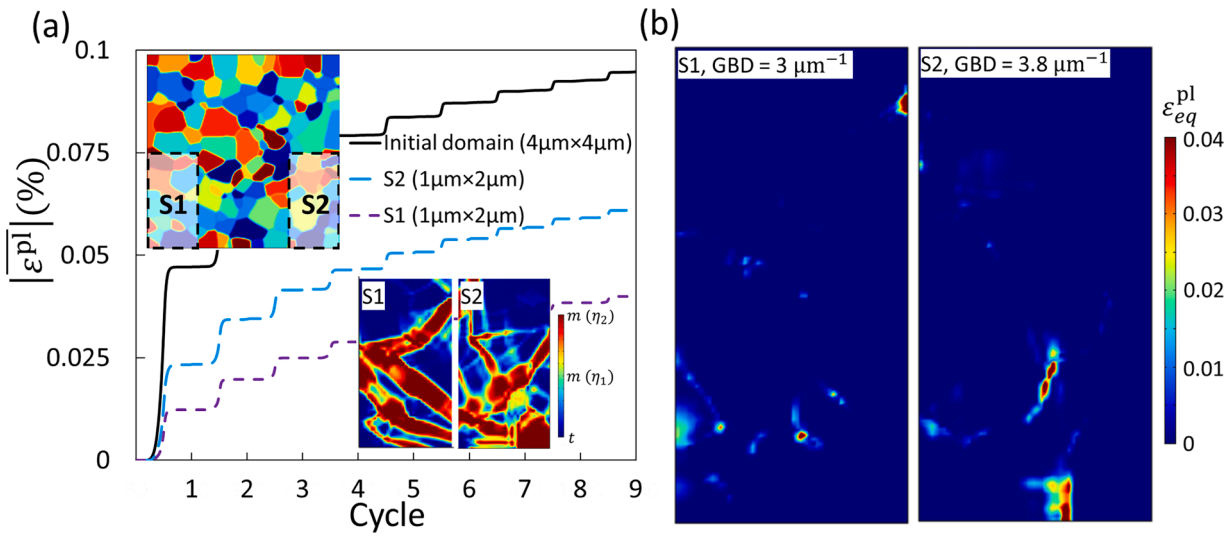

Fig. 5. (a) The PSA in the initial model, S1, and S2 sub domains; Inset-Top) the location of sub domains S1 and S2 in the initial model; Inset-Bottom) the MPT in S1 and S2 at the end of loading of C9;(b) the equivalent plastic strain in S1 and S2 at the end of C9.

increase the average GS, we increased the mobility parameter in Eq. (31) to 30 $Pa^{-1}s^{-1}$. Fig. 6(b, top row) shows the obtained microstructure and grains orientations, where the average GS is ~ 1μm, the total length of the GBs is ~ 33μm, and the GBD is 2.03 μm^{-1}. We study two different cases: RO (θ between 0° and 90°) and texture 1 (TX1) (θ between 0° and 30°). Fig. 6(a) shows plots of $|\overline{\varepsilon^{pl}}|$ for the initial model (GS = 0.35μm, GBD = 5.3 μm^{-1}, RO), coarse-grained microstructure with RO (GS = 1μm, GBD = 2.06 $\frac{1}{\mu m}$, RO), and coarse-grained microstructure with texture (GS = 1μm, GBD = 2.06 μm^{-1}, TX1). Fig. 6(b, bottom row) shows the plastic strain distribution throughout the domain for both coarse-grained cases. The inset figures show the MPT for both coarse-grained cases. Fig. 6 results indicates that by reducing the number of GBs and GBD through increasing the GS, $|\overline{\varepsilon^{pl}}|$ can be significantly mitigated. This observation can be explained based on two concepts; first, by reducing the number of grains in the domain, the number of triple junctions, GBs, and GBD decreases, and this leads to a lower PSA. Second, the GBs are non-transforming regions, and they halt MPT. Therefore, by reducing the number of GBs, the MPT develops larger bands and occurs easier without being stopped at the GBs and this makes the MPT the dominant energy dissipation mechanism in the system, therefore reduces the energy dissipation through plastic deformation.

The TX1 results shows that by reducing the number of GBs as well as tailoring the grains orientation, $|\overline{\varepsilon^{pl}}|$ can be drastically lowered, and this will lead to a significant higher cyclic life. This result can be used as a guide for future experimental studies and design of SMCs.

4.2. *Effects of grain orientations*

The result of TX1 revealed that the grain orientation has a large impact on the PSA. This result guides us to investigate the effects of textures in more detail. In this subsection we investigate the effects of strong textures by considering three different textures in the initial domain (GS = 0.35μm) and compare the results with the case where grains have random orientations between θ = 0° and θ = 90°, presented in Fig. 3 and Fig. 4. In texture 2 (TX2) a random orientation between θ = 0° and θ = 30°, in texture 3 (TX3) a random orientation between θ = 35° and θ = 45°, and in TX4 a random orientation between θ = 60° and θ = 90°, all with respect to the loading direction, is considered for each grain. The same polycrystal microstructure used in previous simulations

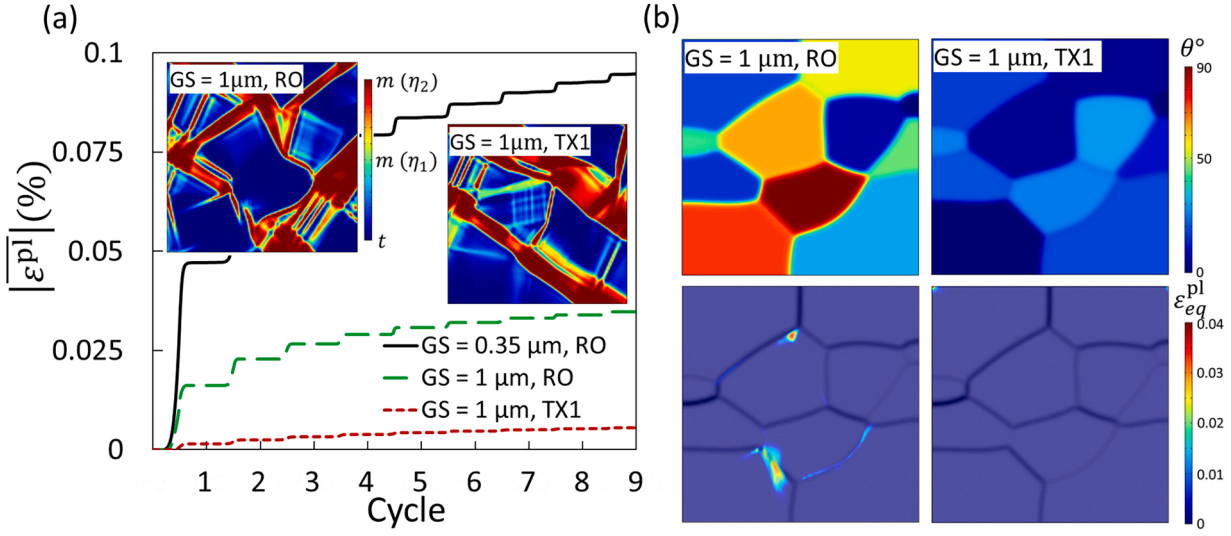

Fig. 6. (a) The PSA versus number of loading cycles; Inset) MPT for RO and TX1 cases at the end of loading of C9; (b) the microstructure and grains orientation (top row), and the equivalent plastic strain in the domains at the end of C9 (bottom row).

is considered.

Fig. 7(a) displays the PSA for different grain orientations of RO, TX2, TX3, and TX4. The inset figures present the MPT distribution map for these textures. By comparing these results to Fig. 4, we can conclude that grain orientation plays a drastic role in PSA and MPT. TX2 leads to a noticeable lower $|\overline{\varepsilon^{pl}}|$, and TX4 leads to a drastically higher $|\overline{\varepsilon^{pl}}|$ compared to RO. In addition, $|\overline{\varepsilon^{pl}}|$ is the lowest in TX2 among all textures. In TX2 and TX3 cases, since most grains are oriented in a direction that MPT happens, a large portion of the elastic energy is dissipated through MPT and not plastic deformation. In addition, both TX2 and TX3 have a lower plastic deformation than the RO case, therefore, a higher cyclic life is expected compared to RO. In TX4 case, the transformed domains are smaller, and they are limited to limited number of grains with angles between 60° to 70° The main mechanism of energy dissipation is plastic deformation, and this leads to a higher PSA and consequently a lower cyclic life before fatigue crack initiation is expected.

4.3. Effects of engineered pores

MPT in zirconia-based SMCs is accompanied by large localized deformations due to phase expansion. If the material is not able to accommodate the large deformations and mismatch stresses, cracks will emerge after few cycles of loading [5–7,69]. In this section, we study the effect of pores on plastic deformation. We first consider a random distribution of pores and then we investigate the effects of pores located closer to GBs. These pores can generate during manufacturing processing or service as a result of volume change due to MPT or high localized stress mainly at GB junctions or around material inclusions [11,70]. Different manufacturing techniques and inclusions can be used to engineer the GBs and inclusions' sites and consequently the location of possible pores [70]. Engineered pores may provide space for phase expansion when the material undergoes MPT and consequently decrease the plastic deformation. We study this hypothesis by considering five different PVF of 0.5%, 1%, 1.5%, 2%, and 2.5%. For PVF of 0.5% and 1% two different pore radiuses (r) of 0.04μm and 0.06μm are considered, and for PVF of 1.5%, 2%, and 2.5% only pores with a radius of 0.06μm are considered. The same microstructure and grain orientation distribution as initial model (Fig. 3) is considered for all cases with pores. Fig. 8(a) shows the plot of $|\overline{\varepsilon^{pl}}|$ for different PVF and pore radiuses; the case labeled "without pores" refers to the initial model shown in Fig. 3 and Fig. 4. Fig. 8(b) presents the plastic strain distribution in the domains with PVF of 0.5% and 1% with different radiuses of 0.04μm and 0.06μm. There is not a noticeable difference in the MPT pattern with pores compared to the initial model shown in Fig. 4. Based on Fig. 8(a), in the most studied cases, the exitance of pores reduces $|\overline{\varepsilon^{pl}}|$, therefore leads to a higher cyclic life. This can be explained based on the fact that pores provide more room for the system to accommodate the expansion due to the MPT and this alleviates the mismatch stresses and reduced the PSA at GBs. However, for the PVF higher than 2 %, $|\overline{\varepsilon^{pl}}|$ increases with a high slop rather than staying flat after cycle 3. Based on the Fig. 8(a), for cases with PVF of 2 % and 2.5 %, $|\overline{\varepsilon^{pl}}|$ even becomes higher than the case with PVF of 1.5 % at the end of C9, and the difference is expected to become larger after C9. These results suggest that pores can reduces the $|\overline{\varepsilon^{pl}}|$, however there is a threshold for the PVF.

As far as pore radius, the smaller radius leads to a lower $|\overline{\varepsilon^{pl}}|$ for the same PVF. This result shows that the number of pores plays a pivotal role. For the same PVF, a smaller pore radius leads to a higher number of pores, which means in more locations over the domain the phase expansion due to MPT can be accommodated and this leads to a lower $|\overline{\varepsilon^{pl}}|$. In addition, these results show that pore radius of 0.04μm is still large enough to accommodate the shape change due to the MPT. In Fig. 8 for all seven cases, pores are randomly distributed over the domain. Since GBs are crucial regions with the highest PSA, we conduct new studies by locating the pores on the GBs with the highest plastic strain. A PVF of 0.5 % at GBs (PVFGBs) and two different pores radiuses of $r = 0.04\mu m$ and $r = 0.06\mu m$ are considered.

Fig. 9(a) shows the plots of $|\overline{\varepsilon^{pl}}|$ for the new cases against the case without pores (the initial model) and the case with PVF = 0.5 % of randomly distributed pores. By locating pores on the GBs, $|\overline{\varepsilon^{pl}}|$ decreases significantly compared to the case with randomly distributed pores. The case of PVFGBs = 0.5 % with $r = 0.04\mu m$ reduces $|\overline{\varepsilon^{pl}}|$ by 30 % with respect to PVF = 0.5 % and $r = 0.04\mu m$, and 38 % with respect to the case without pores. These results confirm that GBs are critical regions and by providing space near GBs to accommodate the phase expansion due to the MPT, the cyclic life before fatigue crack initiation can be increased.

4.4. Analysis of parameters controlling PSA

In this section, we apply a cross-correlation data analysis approach to study the relationship between the microstructural features, the PSA and the MPT fraction (at the end of loading of C9) through a heatmap. To calculate the MPT fraction we use the equation of $\frac{1}{A_{total}}\sum_{i=1}^{2}\eta_i A_i$ where A_i is the area of ith monoclinic variant. The correlation matrix is calculated based on the Pearson approach [71,72] using a correlation coefficient (r) which can vary between -1 and 1. If the value is positive, then it means there is a direct correlation between two variables, meaning by

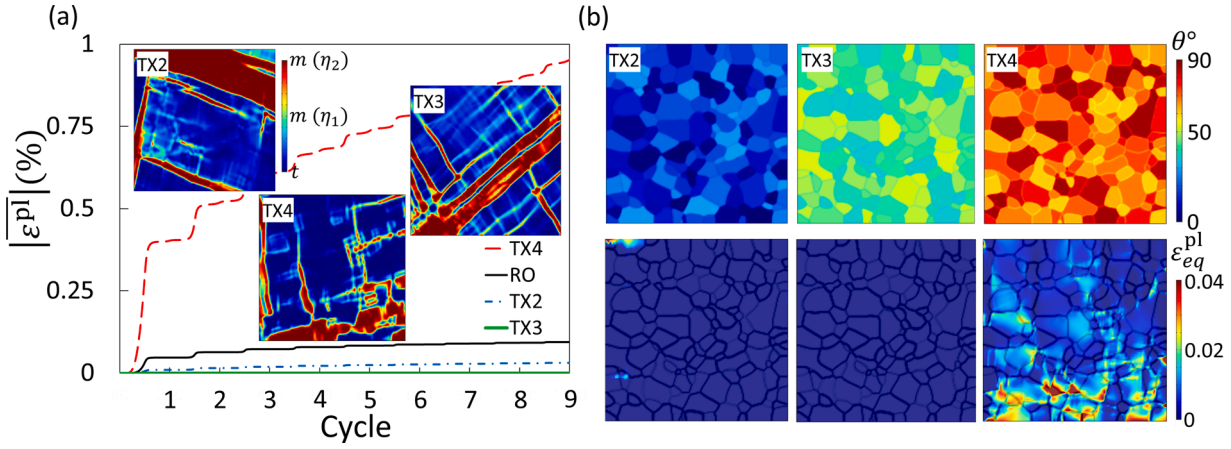

Fig. 7. (a) PSA plots; Inset) MPT for TX2, TX3 and TX4 at the end of loading of C9; (b) TX2, TX4, and TX4 grains orientation (top row), and the equivalent plastic strain in TX2, TX3, and TX4 cases at the end of C9 (bottom row).

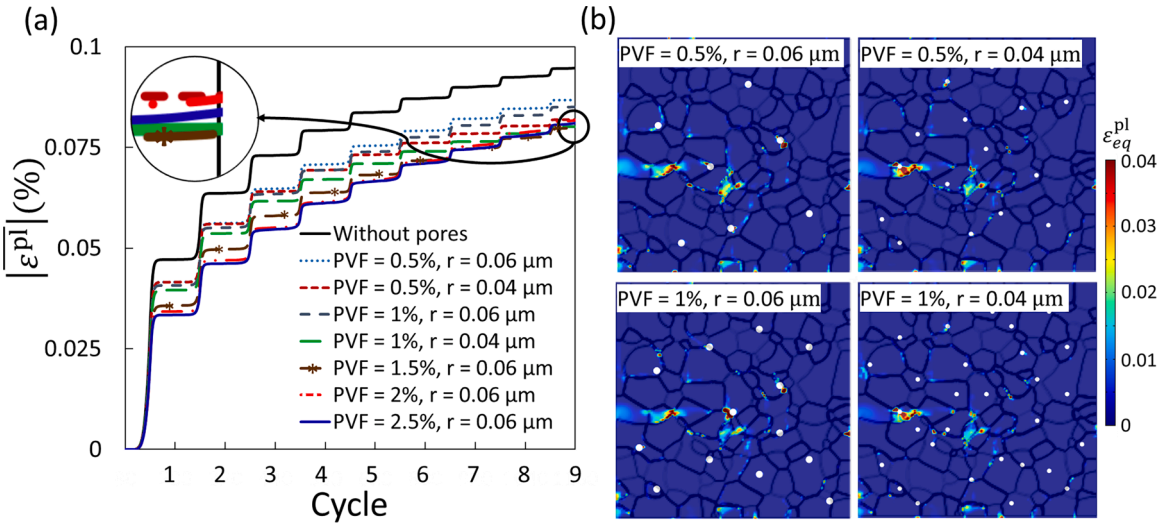

Fig. 8. (a) PSA plots for different PVF and pore size, and (b) equivalent plastic strain in the domains with randomly distributed pores at the end of C9 for 4 different cases.

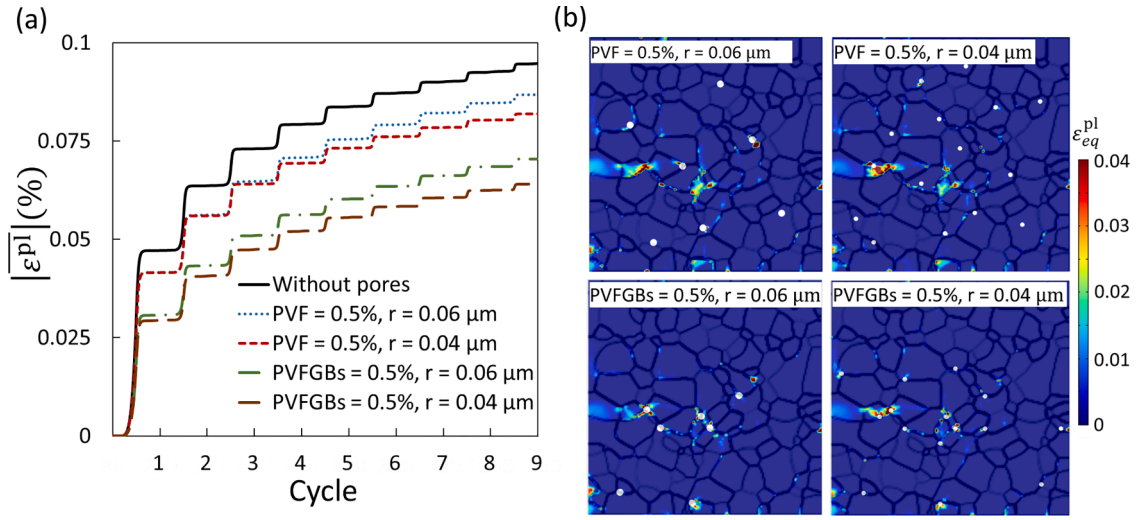

Fig. 9. a) PSA plot; b) the equivalent plastic strain distribution in the domains with randomly distributed pores at the end of C9 (top row) and in the domains with pores located at GBs at the end of C9 (bottom row).

increasing one variable the other variable increases as well. If the value is negative, it means there is an inverse correlation, meaning when one variable increases the other variable decreases. If the value is zero, there is no correlation between the two variables. In addition, if the value is closer to 1 or − 1 there is a stronger positive or negative correlation, respectively. The correlation is calculated based on the below equation:

$$r = \frac{\sum (x_i - \bar{x})(y_i - \bar{y})}{\sqrt{\sum (x_i - \bar{x})^2 \sum (y_i - \bar{y})^2}} \tag{39}$$

x_i are different values of variable x in a sample, $\bar{x}$ is the mean of x_i, y_i are different values of variable y in a sample, and $\bar{y}$ is the mean of y_i.

We consider two target variables of $\left|\overline{\varepsilon^{pl}}\right|$ (at C9) and MPT fraction (at the end of loading of C9), and four attribute variables of pores size (PS), PVF, average grain orientations of textured samples (AGOTX) with respect to loading direction, and GBD. Fig. 10 shows the obtained heatmap.

The plastic deformation and MPT are two energy dissipation mechanisms, and the high negative correlation of −0.6 indicates that only one of them can be the dominant energy dissipation mechanics in a system. The heatmap also shows that the highest correlation is between MPT fraction and the average grain orientations with respect to the loading direction in a textured sample (AGOTX). The correlation is negative (−0.84) which means by increasing the average grain orientation in the textured cases, MPT decreases and therefore MPT would not be the dominant source of energy dissipation and plastic deformation will be the main source of energy dissipation. This is why the heatmap predicts a high positive correlation of 0.78 between AGOTX and $\left|\overline{\varepsilon^{pl}}\right|$. In addition, the heatmap shows a relatively high correlation of 0.42 between GBD and $\left|\overline{\varepsilon^{pl}}\right|$. As expected, this correlation is positive since in the previous sections, we showed that by reducing GBD, $\left|\overline{\varepsilon^{pl}}\right|$ decreases noticeably. Furthermore, the heatmap presents a positive correlation between $\left|\overline{\varepsilon^{pl}}\right|$ and PVF and PS. However, these correlations are small, and this is because based on the results, $\left|\overline{\varepsilon^{pl}}\right|$ can decrease more by changing the AGOTX and GBD compared to applying pores to the system. Based on the previous results in this paper and what the heatmap presents, the AGOTX has the highest effect in controlling $\left|\overline{\varepsilon^{pl}}\right|$, then the GBD plays the most effective role, and next is the pore volume fraction.

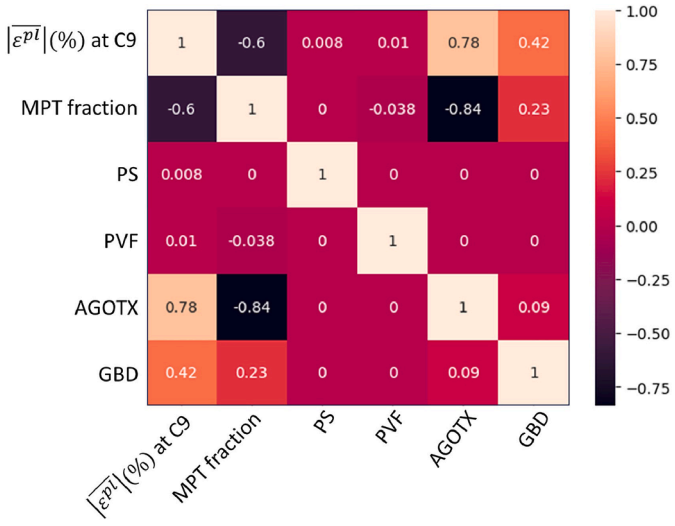

Fig. 10. The correlation between the studied microstructural features and two target variables of $|\overline{\varepsilon^{pl}}|$ (at C9) and MPT fraction (at the end of loading of C9).

5. Conclusions

We integrated a phase-field MPT model with a viscoplasticity model to investigate the effects of microstructural features, such as grains orientation, pores, GBs, as well as domain size on MPT and PSA in polycrystalline SMCs subjected to compressive cyclic loading. We used average PSA as an indicator of cyclic life, aiming to enhance the material's ability to withstand a higher number of cycles before fatigue crack initiation by reducing average PSA.

In these materials, the previous experimental and computational studies have established that the plastic strain originates from irreversible mechanisms such as slip and GB sliding. To simulate plastic strain, we employed a straightforward viscoplasticity model with a few constants that require determination. Our results showed that this model is capable of predicting cyclic plastic strains effectively, aligning quantitatively with available experimental reports.

Our simulations predicted a high plastic strain at the GBs particularly at triple junctions, and this result is consistent with experimental observations. Given that GBs are critical sites with the highest plastic strain, we studied the effects of GBD on PSA. The model predicts a lower PSA if GBD is lowered achieved by domain size reduction or increased average GS. The results on the domain size effects are in good agreement with existing experimental observations. Furthermore, our research reveals that engineered pores can play a more effective role in reducing the PSA when located close to the GBs. This can be attributed to pores offering space to accommodate the expansion due to MPT. However, we have identified a threshold for PVF; if PVF exceeded 2 %, additional porosity may play a negative role and increase PSA and consequently decrease the cyclic life. Our model also captures the impact of grain orientations effectively. Textured microstructures with grains oriented close to 45° with respect to the loading direction exhibited drastic reduction in PSA, primarily due to MPT becoming the dominant energy dissipation mechanism. This phenomenon could lead to significantly enhanced cyclic life in polycrystalline SMCs.

The ideas and simulations presented in this study for reducing PSA in polycrystalline shape memory materials represent novel contributions not explored in previous experimental or computational studies. The primary purpose of this study was to offer insights for future research on tailoring the microstructure to enhance the cyclic life of SMCs. In addition, the model presented in this research is extendable to other polycrystalline shape memory materials.

Data availability

All the results are presented as figures in this paper. The generated datasets through simulations to plot these figures are available from the corresponding author.

CRediT authorship contribution statement

Amirreza Lotfolahpour: Writing – original draft, Validation, Software, Methodology, Investigation, Formal analysis, Data curation, Conceptualization. **Mohsen Asle Zaeem:** Writing – review & editing, Supervision, Project administration, Methodology, Investigation, Funding acquisition, Formal analysis, Conceptualization.

Declaration of competing interest

The authors declare that they have no known competing financial interests or personal relationships that could have appeared to influence the work reported in this paper.

Acknowledgement

This work was supported by the U.S. National Science Foundation, under Award number CMMI 2054274. The authors are grateful for the supercomputing time allocation provided by the NSF's ACCESS (Advanced Cyberinfrastructure Coordination Ecosystem: Services & Support), Award No. DMR140008.

Appendix A

Here we explain the approach used for calculating the GB length and GBD. With the solution to Eq. (31) (the PF polycrystalline model) at hand, we assign a grain orientation to each grain according to Eq. (A1).

$$\theta = \theta_1 \times \zeta_1 + \theta_2 \times \zeta_2 \ldots \theta_{30} \times \zeta_{30}, \tag{A1}$$

where θ_i is the selected orientation for grain *i*.

Now, the GBs are identified with the following equation and dGB field is shown in Fig. A1:

$$\mathrm{dGB} = \sqrt{\left(\frac{d\theta}{dx}\right)^2 + \left(\frac{d\theta}{dy}\right)^2}\ \mathrm{m}^{-1} \tag{A2}$$

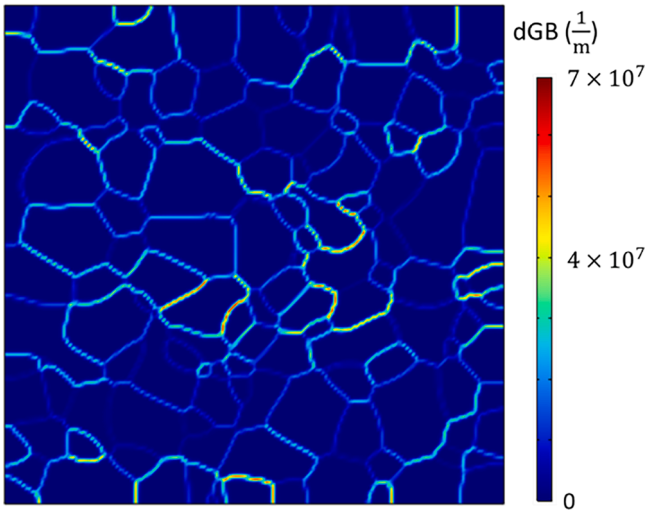

Fig. A1. The distribution of **dGB**.

Eq. (A2) calculates the magnitude of the gradient of θ over the domain, and this equation yields different values for different GBs. The value of dGB depends on the misorientation angle between two neighboring grains. In addition, this number is ~0 inside the grains.

Now, we calculate the minimum value for dGB which we consider representing a GB. First, we consider the steady state problem in a 1D domain with only one OP ζ. Therefore the Eq. (29)–(31) become:

$$F(\zeta(x)) = G\int_V \left(f + \frac{k}{2}(\nabla\zeta(x))^2\right)dV, \tag{A3}$$

$$f = \sum_{i=1}^{s}\left(-\frac{\alpha}{2}\zeta(x)^2 + \frac{\beta}{4}\zeta(x)^4\right), \tag{A4}$$

$$0 = -\alpha\zeta(x) + \beta\zeta(x)^3 - k\nabla^2\zeta(x) \tag{A5}$$

Considering G = 1Pa, α and β equal to 1 (see Table 1), the Eq. (A5) recovers the steady state Allen-Cahn equation [57]. It is worth mentioning that we consider $k = 2 \times 10^{-16}$ m^2 (Table 1). Applying the boundary conditions of $\zeta(+\infty) = +1$ and $\zeta(-\infty) = -1$ yields an analytical solution of $\zeta(x) = \tanh\left(\frac{x}{\sqrt{2k}}\right)$ which is plotted in Fig. A2 in a domain size of 0.2μm. From the profile shown in Fig. A2, we define the width of the smeared interface as the intersection of the tangent line (ζ_t) at $x = 0$ with $\zeta = \pm 1$. This yields an interface width of $2\sqrt{2k} \approx 0.04\mu$m. It is worth noting that this GB thickness is small enough compared to the domain size, and for this microscale study, using a smaller GB thickness does not noticeably affect the results.

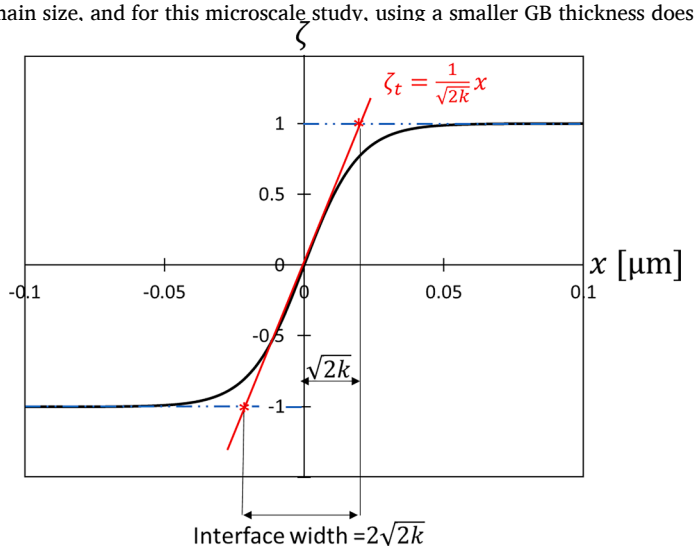

Fig. A2. The analytical solution of Eq. (A5) ($\tanh\left(\frac{x}{\sqrt{2k}}\right)$) and the process of calculating the smeared interface width.

Now, we consider that two grains are separated when they are misoriented by at least $\Delta\theta_{min} = 0.105$ radians over the width of the smeared interface. Therefore, the minimum value of dGB to define a GB is:

$$\mathrm{dGB}_{min} = \frac{\Delta\theta_{min}}{2\sqrt{2k}} = 2.6 \times 10^6 \mathrm{m}^{-1} \tag{A6}$$

By applying the above constraint, the plot of dGB is shown in Fig. A3.

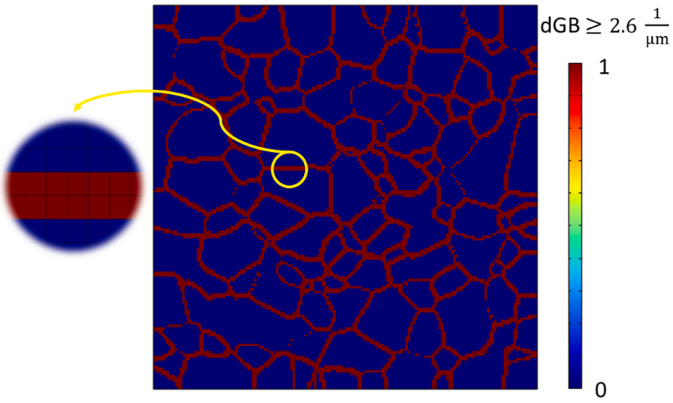

Fig. A3. The distribution of dGB $\geq 2.6 \times 10^6$ m^{-1}.

By integrating dGB over the entire domain we will obtain the total area of dGB. By dividing this area by the size of two elements (based on Fig. A3, the dGB is over two elements for almost all GBs, the size of each element is 0.02μm), we can calculate the total length of GBs. To calculate the GBD, we divide the total length of GBs by the domain area. For example, for the case of Fig. A3, the GB length calculation yields 84μm and GBD is calculated by dividing the GB length by the domain area (16 μm^2) which yields 5.3 μm^{-1}.

References

[1] Otsuka K, Wayman CM. Shape memory materials. Cambridge university press; 1999.
[2] Du Z, Yu H, Schuh CA, Gan CL. Shape memory ceramic particles and structures formed thereof. Google Patents; 2020.
[3] Hang ZY, Hassani-Gangaraj M, Du Z, Gan CL, Schuh CA. Granular shape memory ceramic packings. Acta Mater 2017;132:455–66.
[4] Kelly PM, Rose LF. The martensitic transformation in ceramics—Its role in transformation toughening. Prog Mater Sci 2002;47(5):463–557.
[5] Lai A, Du Z, Gan CL, Schuh CA. Shape memory and superelastic ceramics at small scales. Science 2013;341(6153):1505–8.
[6] Du Z, Zeng XM, Liu Q, Schuh CA, Gan CL. Superelasticity in micro-scale shape memory ceramic particles. Acta Mater 2017;123:255–63.
[7] Camposilvan E, Anglada M. Size and plasticity effects in zirconia micropillars compression. Acta Mater 2016;103:882–92.
[8] Lankford J, Page R, Rabenberg L. Deformation mechanisms in yttria-stabilized zirconia. J Mater Sci 1988;23:4144–56.
[9] Zeng XM, Lai A, Gan CL, Schuh CA. Crystal orientation dependence of the stress-induced martensitic transformation in zirconia-based shape memory ceramics. Acta Mater 2016;116:124–35.
[10] Zhang N, Asle Zaeem M. Competing mechanisms between dislocation and phase transformation in plastic deformation of single crystalline yttria-stabilized tetragonal zirconia nanopillars. Acta Mater 2016;120:337–47.
[11] Cissé C, Asle Zaeem M. Defect-induced asymmetrical mechanical behavior in shape memory zirconia: a phase-field investigation. J Eur Ceram Soc 2022;42(10):4296–310.
[12] Mamivand M, Asle Zaeem M, El Kadiri H. A review on phase field modeling of martensitic phase transformation. Comput Mater Sci 2013;77:304–11.
[13] Kan Q, Zhang Y, Shi W, Xu Y, Yu C, Kang G. Functional fatigue of superelasticity and elastocaloric effect for NiTi springs. Int J Mech Sci 2024;265:108889.
[14] Zhao T, Kang G. Experimental study and life prediction on fatigue failure of NiTi shape memory alloy under multi-axial one-way shape memory cyclic loadings. Int J Fatigue 2022;155:106609.
[15] Sidharth R, Mohammed A, Sehitoglu H. Functional fatigue of NiTi shape memory alloy: effect of loading frequency and source of residual strains. Shape Mem Superelasticity 2022;8(4):394–412.
[16] Zhang Y, Moumni Z, You Y, Zhang W, Zhu J, Anlas G. Multiscale TRIP-based investigation of low-cycle fatigue of polycrystalline NiTi shape memory alloys. Int J Plast 2019;115:307–29.
[17] Wan V, MacLachlan D, Dunne F. A stored energy criterion for fatigue crack nucleation in polycrystals. Int J Fatigue 2014;68:90–102.
[18] Manonukul A, Dunne F. High–and low–cycle fatigue crack initiation using polycrystal plasticity. Proc R Soc Lond A Math Phys Eng Sci 2004;460(2047):1881–903.
[19] Esfahani SE, Ghamarian I, Levitas VI, Collins PC. Microscale phase field modeling of the martensitic transformation during cyclic loading of NiTi single crystal. Int J Solids Struct 2018;146:80–96.
[20] Cissé C, Asle Zaeem M. Design of NiTi-based shape memory microcomposites with enhanced elastocaloric performance by a fully thermomechanical coupled phase-field model. Mater Des 2021;207:109898.
[21] Xie X, Kang G, Kan Q, Yu C. Phase-field theory based finite element simulation on thermo-mechanical cyclic deformation of polycrystalline super-elastic NiTi shape memory alloy. Comput Mater Sci 2020;184:109899.
[22] Cissé C, Asle Zaeem M. An asymmetric elasto-plastic phase-field model for shape memory effect, pseudoelasticity and thermomechanical training in polycrystalline shape memory alloys. Acta Mater 2020;201:580–95.
[23] Lotfolahpour A, Huber W, Asle Zaeem M. A phase-field model for interactive evolution of phase transformation and cracking in superelastic shape memory ceramics. Comput Mater Sci 2023;216:111844.
[24] Mamivand M, Asle Zaeem M, El Kadiri H, Chen LQ. Phase field modeling of the tetragonal-to-monoclinic phase transformation in zirconia. Acta Mater 2013;61(14):5223–35.
[25] Cissé C, Asle Zaeem M. A phase-field model for non-isothermal phase transformation and plasticity in polycrystalline yttria-stabilized tetragonal zirconia. Acta Mater 2020;191:111–23.
[26] Asle Zaeem M, Zhang N, Mamivand M. A review of computational modeling techniques in study and design of shape memory ceramics. Comput Mater Sci 2019;160:120–36.
[27] Mamivand M, Asle Zaeem M, El Kadiri H. Shape memory effect and pseudoelasticity behavior in tetragonal zirconia polycrystals: a phase field study. Int J Plast 2014;60:71–86.
[28] Yu C, Kang G, Kan Q, Song D. A micromechanical constitutive model based on crystal plasticity for thermo-mechanical cyclic deformation of NiTi shape memory alloys. Int J Plast 2013;44:161–91.
[29] Yu C, Kang G, Kan Q. Crystal plasticity based constitutive model of NiTi shape memory alloy considering different mechanisms of inelastic deformation. Int J Plast 2014;54:132–62.
[30] Yu C, Kang G, Kan Q. A micromechanical constitutive model for anisotropic cyclic deformation of super-elastic NiTi shape memory alloy single crystals. J Mech Phys Solids 2015;82:97–136.
[31] Yu C, Kang G, Kan Q, Xu X. Physical mechanism based crystal plasticity model of NiTi shape memory alloys addressing the thermo-mechanical cyclic degeneration of shape memory effect. Mech Mater 2017;112:1–17.
[32] Paranjape HM, Manchiraju S, Anderson PM. A phase field–Finite element approach to model the interaction between phase transformations and plasticity in shape memory alloys. Int J Plast 2016;80:1–18.
[33] Paranjape HM, Bowers ML, Mills MJ, Anderson PM. Mechanisms for phase transformation induced slip in shape memory alloy micro-crystals. Acta Mater 2017;132:444–54.
[34] Xie X, Kang G, Kan Q, Yu C, Peng Q. Phase field modeling for cyclic phase transition of NiTi shape memory alloy single crystal with super-elasticity. Comput Mater Sci 2018;143:212–24.
[35] Xie X, Kang G, Kan Q, Yu C, Peng Q. Phase field modeling to transformation induced plasticity in super-elastic NiTi shape memory alloy single crystal. Model Simul Mater Sci Eng 2019;27(4):045001.
[36] Xu B, Kang G, Kan Q, Yu C, Xie X. Phase field simulation on the cyclic degeneration of one-way shape memory effect of NiTi shape memory alloy single crystal. Int J Mech Sci 2020;168:105303.
[37] Ju X, Moumni Z, Zhang Y, Zhang F, Zhu J, Chen Z, Zhang W. A multi-physics, multi-scale and finite strain crystal plasticity-based model for pseudoelastic NiTi shape memory alloy. Int J Plast 2022;148:103146.
[38] Bo Z, Lagoudas DC. Thermomechanical modeling of polycrystalline SMAs under cyclic loading, Part III: evolution of plastic strains and two-way shape memory effect. Int J Eng Sci 1999;37(9):1175–203.

[39] Wang J, Moumni Z, Zhang W. A thermomechanically coupled finite-strain constitutive model for cyclic pseudoelasticity of polycrystalline shape memory alloys. Int J Plast 2017;97:194–221.
[40] Ebrahimi P, Arghavani J, Naghdabadi R, McGarry JP. On the effect of detwinning-induced plasticity in compressive cyclic loading of NiTi shape memory alloys. Mech Mater 2020;148:103451.
[41] Xu B, Yu C, Kan Q, Kang G. Phase field study on the microscopic mechanism of the cyclic degradation of shape memory effect in nano-polycrystalline NiTi shape memory alloys. Eur J Mech A Solids 2022;93:104544.
[42] Chaugule PS, le Graverend JB. Crystal-plasticity modeling of phase transformation–viscoplasticity coupling in high-temperature shape memory alloys. Int J Plast 2022;153:103243.
[43] Kan Q, Shi W, Song D, Yu C, Kang G. A micromechanical constitutive model of high-temperature shape memory alloys. Int J Mech Sci 2023;251:108328.
[44] Karamooz-Ravari MR, Andani MT, Kadkhodaei M, Saedi S, Karaca H, Elahinia M. Modeling the cyclic shape memory and superelasticity of selective laser melting fabricated NiTi. Int J Mech Sci 2018;138:54–61.
[45] Xiao Y, Jiang D. Constitutive modelling of transformation pattern in superelastic NiTi shape memory alloy under cyclic loading. Int J Mech Sci 2020;182:105743.
[46] Simoes M, Martínez-Pañeda E. Phase field modelling of fracture and fatigue in shape memory alloys. Comput Methods Appl Mech Eng 2021;373:113504.
[47] Simoes M, Braithwaite C, Makaya A, Martínez-Pañeda E. Modelling fatigue crack growth in shape memory alloys. Fatigue Fract Eng Mater Struct 2022;45(4):1243–57.
[48] Woodworth LA, Kaliske M. A temperature dependent constitutive model for functional fatigue in shape memory alloys. Mech Mater 2022;165:104126.
[49] Zhang X, Yan X, Xie H, Sun R. Modeling evolutions of plastic strain, maximum transformation strain and transformation temperatures in SMA under superelastic cycling. Comput Mater Sci 2014;81:113–22.
[50] Bingham EC. An investigation of the laws of plastic flow. US Government Printing Office; 1917.
[51] Sun Y, Luo J, Zhu J, Zhou K. A non-isothermal phase field study of the shape memory effect and pseudoelasticity of polycrystalline shape memory alloys. Comput Mater Sci 2019;167:65–76.
[52] Zhong Y, Zhu T. Phase-field modeling of martensitic microstructure in NiTi shape memory alloys. Acta Mater 2014;75:337–47.
[53] Xu B, Kang G, Yu C, Kan Q. Phase field simulation on the grain size dependent super-elasticity and shape memory effect of nanocrystalline NiTi shape memory alloys. Int J Eng Sci 2020;156:103373.
[54] Zhang Y, Jin X, Hsu T. Thermodynamic calculation of Ms in ZrO2–CeO2–Y2O3 system. J Eur Ceram Soc 2003;23(5):685–90.
[55] Huber W, Asle Zaeem M. A mixed mode phase-field model of ductile fracture. J Mech Phys Solids 2023;171:105123.
[56] Landau LD. Collected papers of ld landau. Pergamon; 1965.
[57] Allen SM, Cahn JW. A microscopic theory for antiphase boundary motion and its application to antiphase domain coarsening. Acta Metall 1979;27(6):1085–95.
[58] E.A. de Souza Neto, D. Peric, D.R. Owen, Computational methods for plasticity: theory and applications, John Wiley & Sons2011.
[59] Kuhn HW, Tucker AW. Nonlinear programming, traces and emergence of nonlinear programming. Springer; 2013. p. 247–58.
[60] Asle Zaeem M, El Kadiri H, Wang PT, Horstemeyer MF. Investigating the effects of grain boundary energy anisotropy and second-phase particles on grain growth using a phase-field model. Comput Mater Sci 2011;50(8):2488–92.
[61] Hofacker M, Miehe C. Continuum phase field modeling of dynamic fracture: variational principles and staggered FE implementation. Int J Fract 2012;178(1):113–29.
[62] Keuper M, Berthold C, Nickel KG. Long-time aging in 3mol.% yttria-stabilized tetragonal zirconia polycrystals at human body temperature. Acta Biomater 2014;10(2):951–9.
[63] Zhao XS, Shang SL, Liu ZK, Shen JY. Elastic properties of cubic, tetragonal and monoclinic ZrO2 from first-principles calculations. J Nucl Mater 2011;415(1):13–7.
[64] Chan SK, Fang Y, Grimsditch M, Li Z, Nevitt MV, Robertson WM, Zouboulis ES. Temperature dependence of the elastic moduli of monoclinic zirconia. J Am Ceram Soc 1991;74(7):1742–4.
[65] Moshkelgosha E, Mamivand M. Three-dimensional phase field modeling of fracture in shape memory ceramics. Int J Mech Sci 2021;204:106550.
[66] Ren K, Xia J, Wang Y. Grain growth kinetics of 3mol.% yttria-stabilized zirconia during flash sintering. J Eur Ceram Soc 2019;39(4):1366–73.
[67] Zhang Y, You Y, Moumni Z, Anlas G, Zhu J, Zhang W. Experimental and theoretical investigation of the frequency effect on low cycle fatigue of shape memory alloys. Int J Plast 2017;90:1–30.
[68] Song D, Yu C, Zhang C, Kang G. Superelasticity degradation of NiTi shape memory alloy in wide ranges of temperature and loading level: experimental observation and micromechanical constitutive model. Int J Plast 2023;161:103487.
[69] Du Z, Zeng XM, Liu Q, Lai A, Amini S, Miserez A, Schuh CA, Gan CL. Size effects and shape memory properties in ZrO2 ceramic micro-and nano-pillars. Scr Mater 2015;101:40–3.
[70] Sarker S, Mumu HT, Al-Amin M, Alam MZ, Gafur M. Impacts of inclusion of additives on physical, microstructural, and mechanical properties of Alumina and Zirconia toughened alumina (ZTA) ceramic composite: a review. Mater Today Proc 2022;62:2892–918.
[71] Pearson K. Mathematical contributions to the theory of evolution.—III. Regression, heredity, and panmixia. Philos Trans R Soc A 1896;(187):253–318. of London. Series A, containing papers of a mathematical or physical character.
[72] Rodgers JLee, Nicewander WA. Thirteen ways to look at the correlation coefficient. Am Stat 1988;42(1):59–66.